

# Numerical Simulation of the Sudden Rainstorm Associated with the Remnants of Typhoon Meranti (2010)

ZHOU Lingli<sup>1,2</sup> (周玲丽), DU Huiliang<sup>2</sup> (杜惠良), ZHAI Guoqing<sup>3</sup> (翟国庆),  
and WANG Donghai<sup>1</sup> (王东海)

<sup>1</sup>State Key Laboratory of Severe Weather, Chinese Academy of Meteorological Sciences, Beijing 100081

<sup>2</sup>Zhejiang Province Meteorological Observatory, Hangzhou 310017

<sup>3</sup>Department of Earth Sciences, Zhejiang University, Hangzhou 310027

(Received 15 June 2012; revised 16 November 2012; accepted 29 November 2012)

## ABSTRACT

The Advanced Research Weather Forecasting (ARW) model was used to simulate the sudden heavy rainstorm associated with the remnants of Typhoon Meranti in September 2010. The results showed that the heavy rainfall was produced when the remnant clouds redeveloped suddenly, and the redevelopment was caused by rapid growth of micro/mesoscale convective systems (MCSs). As cold air intruded into the warm remnant clouds, the atmosphere became convectively unstable and frontogenesis happened due to strong wind shear between weak northerly flow and strong southwesterly flow in the lower levels. Under frontogenesis-forcing and warm-air advection stimulation in updrafts, vertical convection developed intensely inside the remnant clouds, with MCSs forming and maturing along the front. The genesis and development of MCSs was due to the great progress vertical vorticity made. The moist isentropic surface became slantwise as atmospheric baroclinity intensified when cold air intruded, which reduced the convective instability of the air. Meanwhile, vertical wind shear increased because the north cold air caused the wind direction to turn from south to north with height. In accordance with slantwise vorticity development (SVD), vertical vorticity would develop vigorously and contribute greatly to MCSs. Buoyancy, the pressure gradient, and the lifting of cold air were collectively the source of kinetic energy for rainfall. The low-level southwesterly jet from the western margin of the Western Pacific Subtropical High transported water and heat to remnant clouds. Energy bursts and continuous water vapor transportation played a major role in producing intense rainfall in a very short period of time.

**Key words:** remnant clouds, heavy rainfall, frontogenesis, vertical convection, slantwise vorticity development, kinetic energy budget

**Citation:** Zhou, L. L., H. L. Du, G. Q. Zhai, and D. H. Wang, 2013: Numerical simulation of the sudden rainstorm associated with the remnants of Typhoon Meranti (2010). *Adv. Atmos. Sci.*, **30**(5), 1353–1372, doi: 10.1007/s00376-012-2127-3.

## 1. Introduction

Tropical cyclones (TCs) often bring about torrential rains during landfall (Chen, 2006; Cheng et al., 2007). One of the reasons for most TCs weakening quickly into remnant clouds after landfall is that the surface friction consumes the kinetic energy input in the lower levels significantly and cuts off inflows. The rainfall will then decrease correspondingly because the moisture conditions at the underlying surface become

poorer after the TC makes landfall (Chen and Meng, 2001; Dong et al., 2010). However, some studies have shown that typhoon remnants could revive and produce even heavier rainfall than was the case at landfall under the interaction of moisture transfer from the ITCZ, favorable topographic conditions, and micro/mesoscale convective systems (MCSs), when typhoon circulation combines with mid-latitude weather systems (Chen and Luo, 2004; Duan and Chen, 2005; Han et al., 2007; Li et al., 2008). For instance, 0009

---

\*Corresponding author: ZHOU Lingli, zhoulingli1231@gmail.com

tropical depression (TD) produced accumulated rainfall of 264 mm within 12 hours in the Xujiahui area of Shanghai, China (Qi and Zhao, 2004; Du et al., 2007; Yang et al., 2011). In 2006, the intensity of Tropical Storm BILIS barely reached the category of typhoon when it made landfall, and weakened into a TD rapidly thereafter. Nonetheless, it caused heavy rains in most parts of southwestern China, with maximum rainfall exceeding 500 mm (Gao et al., 2009). Typhoon Neoguri (0801) caused much heavier rain in Guangdong Province after being downgraded to a TD over land than it did during landfall (Zhang et al., 2009). Dong et al. (2010) analyzed all cases of typhoon rainfall reinforcement after landfall in China from 1949 to 2006 and found that more than 80% of cases were associated with TD remnant clouds weakened from typhoons. The authors also found that there has been a rising trend of remnant-cloud rain-reinforcement in recent years, although the overall frequency of the phenomenon historically is not high, accounting for just 9.7% of all typhoons. Currently, there is no sufficient forecasting technique for this kind of rainstorm. There is a tendency to miss or underestimate such rain events, creating a barrier for disaster prevention and mitigation and posing a serious threat to the lives and properties of people living in affected areas.

A few meteorologists have been aware of the situation and have carried out research on the reinforcement of remnant cloud rainstorms. The continual development and turnover of mesoscale convective clusters inside a TD is the direct creator of the rainstorm (Qi and Zhao, 2004). Yang et al. (2003) suggested a vertical circulation develops before a TD rainstorm, and the reason for reintensification of the TD is that it moves into a large-scale convergent environment favorable for the conversion from convergence to positive vorticity tendency under the effect of the Coriolis force (Yang et al., 2011). Bosart and Dean (1991) proposed that the interaction between cyclonic vorticity advection from the upper-level westerly trough and low-level remnant clouds furthers the genesis of the front to produce rainfall reinforcement. Du et al. (2007) found that the second kind of thermal wind helicity can reflect well the heavy rainfall area and evolution over time associated with the TD. Kong (2002) considered that water surfaces such as large lakes, reservoirs and saturated wetlands can transport vapor upward into the stagnated remnant clouds to sustain, or even intensify, the system to cause rain growth. Besides, the vertical shear of wind, warm air advection, front genesis, topography, and latent heat transport in the boundary layer, can also play an important role in the strength and occurrence of precipitation (Yan et al., 2005; Gao et al., 2009).

However, most studies have focused mainly on historical statistical analysis, synoptic-scale diagnosis, or mesoscale phenomena of the rainstorm. The physical mechanisms for redevelopment of the remnant clouds, the genesis and intensification of the MCSs internal to the system, and the kinetic energy mechanisms for such heavy rainfall events to occur in so short a period of time have yet to be fully discussed. In this context, the aim of the present reported work was to study, by numerical simulation using Weather Research Forecasting model (WRF) and WRF Variational data assimilation system (WRF-Var), a torrential rainstorm associated with the remnant clouds of typhoon Meranti (2010) that occurred within six hours of landfall in southern Hangzhou, Zhejiang Province, China. Section 2 provides a general overview of the synoptic situation and rain event. The design of the numerical simulation and verification of the results are presented in section 3. Section 4 analyzes the external environmental conditions favorable for remnant-cloud redevelopment and rainfall, which is followed by an examination of the mesoscale features of the MCS in section 5. Section 6 analyzes the moisture potential vorticity (MPV) of the MCSs in an attempt to elucidate the internal physical mechanism of MCS genesis. In section 7 we compute the kinetic energy budget equation to analyze the kinetic energy source of the development of the rainstorm. Finally, a discussion of the overall findings is given in section 8.

## 2. Synoptic situation and overview of the rainstorm

TC Meranti was born over the ocean southeast of Taiwan Island in China in September 2010. At 1930 UTC 09 September 2010, Meranti was upgraded to typhoon status and made landfall on the eastern coast of Shishi in Fujian Province. The intensity of Meranti then declined rapidly into a TD, and the National Meteorological Center of China stopped preparations and reporting of Meranti at 1800 UTC 11 September 2010 (Du et al., 2011). However, TD Meranti did not die out soon after landfall, but instead the remnant clouds sustained for more than 10 hours (Fig. 1a). Unfortunately, the local meteorological department did not expect the subsequent sudden intensification of the remnant clouds and no warming was released before the rainstorm that followed.

300-hPa temperature and geopotential height fields show that there was strong cold air mass in the north of the 40°N area, and the core temperature of the cold air was below  $-40^{\circ}\text{C}$  (Fig. 1b). At 500 hPa (Fig. 1c), the cold air spilled south into North China when the westerly trough moved eastward, and at the same

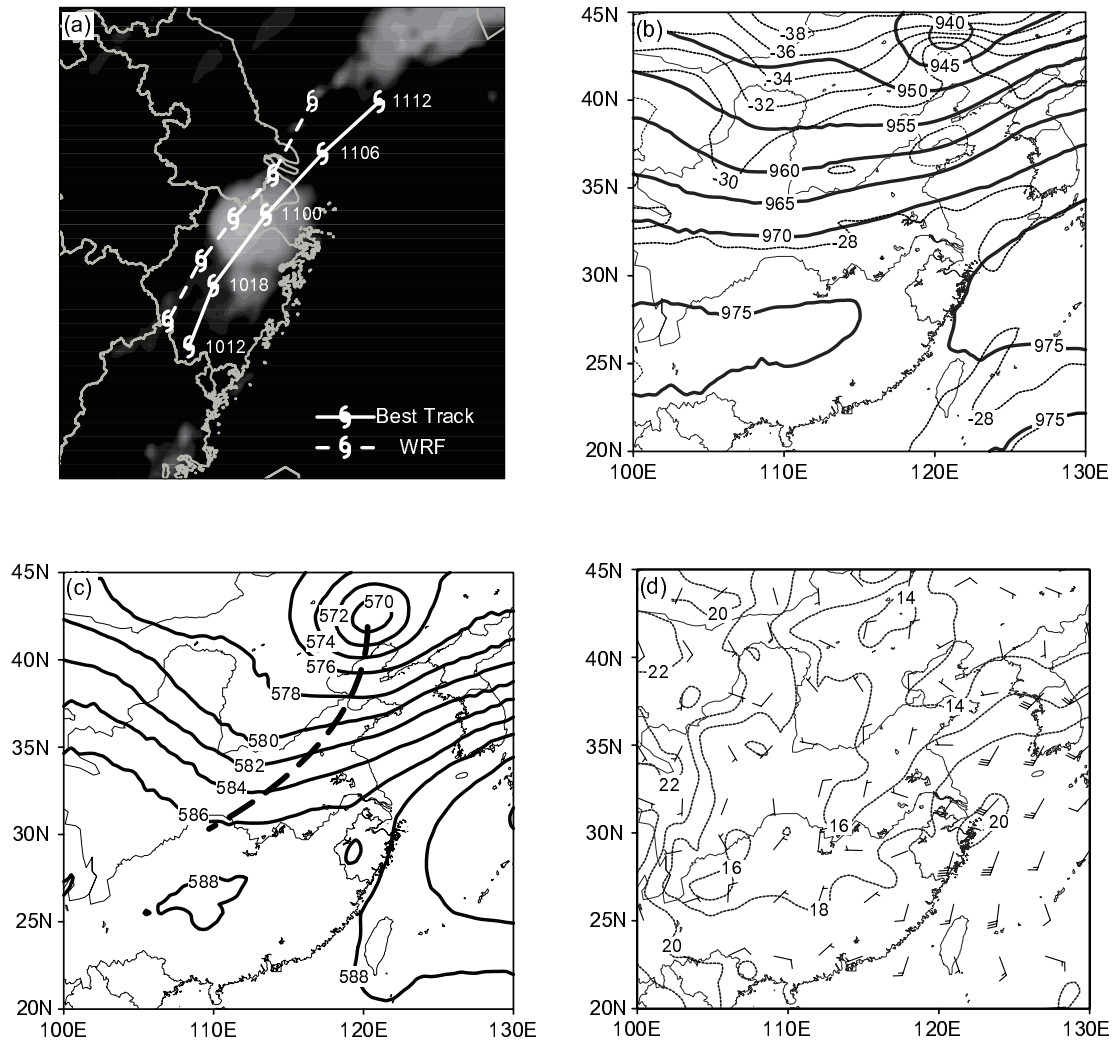


**Fig. 1.** Synoptic situation on the eve of the rainstorm. (a) Infrared cloud image from FY2D at 0100 UTC 11 September 2010, best track data from the China Meteorological Administration (CMA) (solid lines), and simulated track of D01 (dashed lines) from 1200 UTC 10 to 1200 UTC 11 September 2010. (b) The 300-hPa temperature (dotted lines, contour interval of  $2^{\circ}\text{C}$ ) and geopotential height (solid lines, contour interval of 5 gpm) at 1800 UTC 10 September 2010. (c) The 500-hPa geopotential height (solid lines, contour interval of 20 gpm) at 1800 UTC 10 September 2010. The bold dashed line represents the westerly trough. (d) The 850-hPa temperature (solid lines, contour interval of  $2^{\circ}\text{C}$ ) and wind barb vectors at full barb of  $5\text{ m s}^{-1}$  at 1800 UTC 10 September 2010.

time, the remnant clouds moved northward, passing through Zhejiang Province from south to north in the guide of the southwesterly flow on the western margin of the Western Pacific Subtropical High. After the cold air from upper layers intruded into lower levels, it became very weak, with a lowest temperature of  $14^{\circ}\text{C}$ . When the weak cold air invaded the low-level southwesterly jet at 850 hPa, which transported plenty of water vapor from the ocean to the remnant clouds to benefit its maintenance or even revival, strong con-

vection would have been triggered to produce heavy rainfall (Fig. 1d).

From 2100 UTC 10 September 2010 to 0400 UTC 11 September 2010, the cities of Hangzhou and Jiaxing in the north of Zhejiang Province suffered an extreme local rainstorm. The rainfall was very centralized and intense. The accumulated rainfall recorded by the Automatic Weather Station (AWS) at Baima Lake in southern Hangzhou reached 218.9 mm in only three hours (Fig. 2), causing serious urban waterlog-

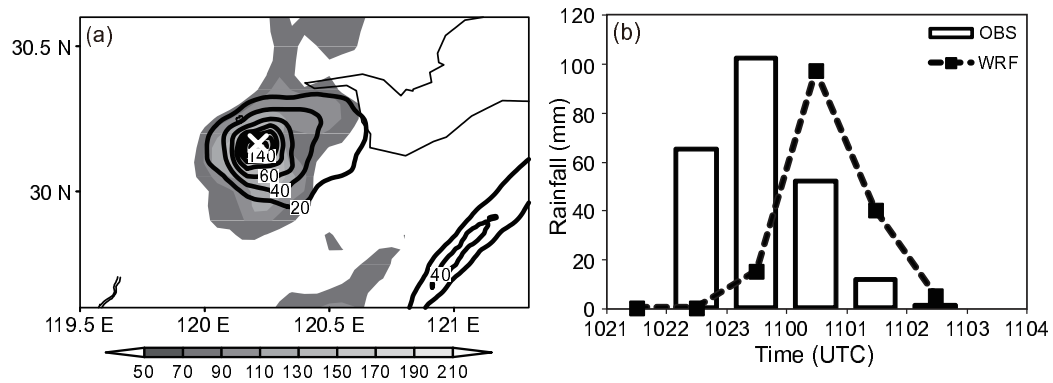


**Fig. 2.** Precipitation that occurred from 2100 UTC 10 to 0400 UTC 11 September 2010. (a) Accumulated precipitation of Automatic Weather stations (AWS) (gray shadowing, contour interval of 30 mm) and simulated total rainfall of D04 (solid lines, contour interval of 20 mm) at Baima Lake. The white cross represents the position of Baima Lake. (b) Hourly AWS precipitation (histogram) and simulated rainfall of D04 (dashed line chart) at Baima Lake.

ging and great financial losses.

### 3. Model description and experimental design

Given the small scale, short duration and high intensity of the rain event, neither the spatial nor temporal resolution of existing observation data are adequate for further study. Therefore, the Advanced Research WRF (ARW) modeling system was used to conduct a mesoscale numerical simulation of the rainstorm. ARW, with its four two-way nested domains and 28 vertical levels in the terrain-following  $\sigma$  coordination, performed a 24-hour simulation, starting from 1200 UTC 10 September 2010. The initial and lateral boundary conditions were based on the six-hourly (0000, 0600, 1200, 1800 UTC) grib2 data from the National Centers for Environmental Prediction (NCEP), with a resolution of  $0.5^\circ \times 0.5^\circ$ . The horizontal grid spacing of the first mesh was 27 km, with 71 (lon)  $\times$  78 (lat) grid points. The horizontal grid spacing of the second mesh was 9 km, with 100 (lon)  $\times$  103 (lat) grid points. The horizontal grid spacing of the third mesh was 3 km, with 202 (lon)  $\times$  193 (lat) grid points. And the horizontal grid spacing of the finest, fourth mesh was 1 km, with 364 (lon)  $\times$  313 (lat) grid points (Fig. 3). The model outputted simulation results every one hour, every 15 minutes, and every five minutes from the first two meshes, the third mesh, and the fourth mesh, respectively. Observation nudging was activated during modeling to make use of the AWS, surface and upper air observation data. Furthermore, inversion data of mid-upper troposphere humidity from the FY2D satellite were assimilated by WRF-Var for better performance. The microphysics process used in the model was the Lin et al. (1983) scheme

(Rutledge and Hobbs, 1984; Tao, 1989). The cumulus option was parameterized with the Betts–Miller–Janjic scheme (Betts, 1986; Betts and Miller, 1986; Janjic, 1994) for the first two meshes, and the Yonsei University boundary layer scheme (Hong and Dudhia, 2003) was adopted.

Figure 1a shows the best track from China Meteorological Administration (CMA) data and the simulated track of the first nested domain (D01) from the model. The simulated TD moved northeastward, the same as the observed TD, but was 50 km farther west than the latter. Furthermore, the simulated TD moved about two hours slower than the observed TD after 1800 UTC 10 September 2010. Figure 2 shows a

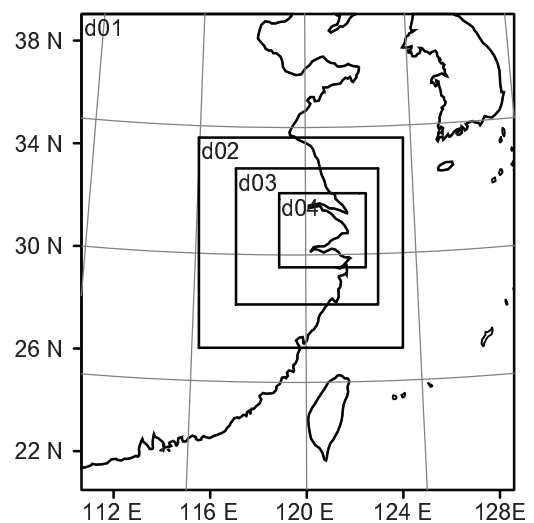


**Fig. 3.** The four nested domains (D01, D02, D03, D04) for the simulation.

comparison between AWS data and simulated rainfall. From Fig. 2a, it can be seen that the simulated rain center was almost coincident with the AWS rain center, both of which were located near Baima Lake to the south of the Qiantang River estuary. The rainfall range from AWS data and the model were also almost the same, at a radius of about 50 km around Baima Lake. The maximum rainfall amount of the simulation results was nearly 40 to 50 mm less than that recorded by the AWS (about 200 mm). Furthermore, the peak time of hourly rainfall from the model appeared between 0000 and 0100 UTC 11 September 2010, about two hours later than according to AWS data (Fig. 2b), which was probably due to the slower movement of the simulated TD compared to the observed TD. In spite of these discrepancies, the overall model results were quite encouraging.

#### 4. External environmental conditions

##### 4.1 Frontogenesis

The remnant clouds of TD Meranti produced extremely heavy rainfall exceeding 200 mm within six hours. Such high precipitation efficiency needs abundant water vapor and intense energy sources. Figure 4 shows significant asymmetry of water vapor flux at 700 hPa in the early stage of the rainstorm. In the eastern part of Zhejiang Province, the maximum water vapor flux reached  $160 \text{ g cm}^{-1} \text{ hPa}^{-1} \text{ s}^{-1}$  under the influence

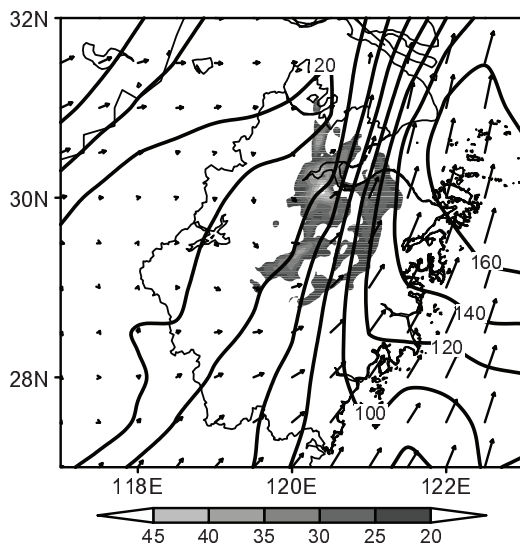


**Fig. 4.** The 700-hPa horizontal water vapor flux (solid lines, contour interval of  $20 \text{ g cm}^{-1} \text{ hPa}^{-1} \text{ s}^{-1}$ ) and wind vectors at the maximum vector value of  $20 \text{ m s}^{-1}$  at 0000 UTC 11 September 2010. The gray shadows represent areas of radar reflectivity larger than 35 dBZ.

of the warm, moist, low-level southwesterly jet, while the water vapor flux in the western part of Zhejiang Province was only  $20 \text{ g cm}^{-1} \text{ hPa}^{-1} \text{ s}^{-1}$  due to the invasion of weak, cold, dry air from the upper levels. The great contrast in water vapor flux between east and west produced a steep gradient from south to north, along which MCS activities were taking place.

The steep gradient of water vapor flux at 700 hPa was favorable for frontogenesis. Some research (Xu et al., 2009) has suggested that the moisture front is in favor of the genesis and development of MCSs, which can be captured and sustained for a while by the front. The quasi-geostrophic frontogenesis function can be expressed as

$$\frac{d}{dt} |\nabla\theta| = \frac{1}{|\nabla\theta|} (\mathbf{Q} \cdot \nabla\theta), \quad (1)$$

where the  $\mathbf{Q}$  vector is defined as

$$\mathbf{Q} = \left( -\frac{\partial \mathbf{V}_g}{\partial x} \cdot \nabla\theta \mathbf{i}, -\frac{\partial \mathbf{V}_g}{\partial y} \cdot \nabla\theta \mathbf{j} \right), \quad (2)$$

by Hoskins et al. (1978) and Hoskins and Pedder (1980).  $\theta$  is potential temperature and  $\mathbf{V}_g$  is geostrophic wind vector.

The quasi-geostrophic frontogenesis function was calculated by Eqs. (1) and (2) and the 700-hPa results are given in Fig. 5. At 1012 UTC 10 September 2010 (Fig. 5a), there was distinct frontogenesis to the northwest of Zhejiang, but frontolysis in most part of northern Zhejiang. The front moved southeastward, approaching Hangzhou Bay where the rainstorm occurred after six hours, and crossed Zhejiang Province from north to south (Fig. 5b). At around 1100 UTC 11 September 2010, the front arrived at Baima Lake and strengthened significantly (Fig. 5c), which was when and where the heaviest rainfall occurred. After that, the front continued to move out to the ocean and the area near Hangzhou Bay experienced frontolysis again (Fig. 5d). The results of the quasi-geostrophic frontogenesis function demonstrates that the cold dry air travelling from the upper levels and the warm moist air from the low-level southwesterly jet contributed to strong frontogenesis, and the front was pushed from northwest to southeast by the cold dry air as it intruded into Zhejiang Province. Under the frontogenetic forcing, MCSs formed and developed intensely (Fig. 4).

There is another expression of Eq. (1) in terms of divergence, stretching deformation and shear deforma-

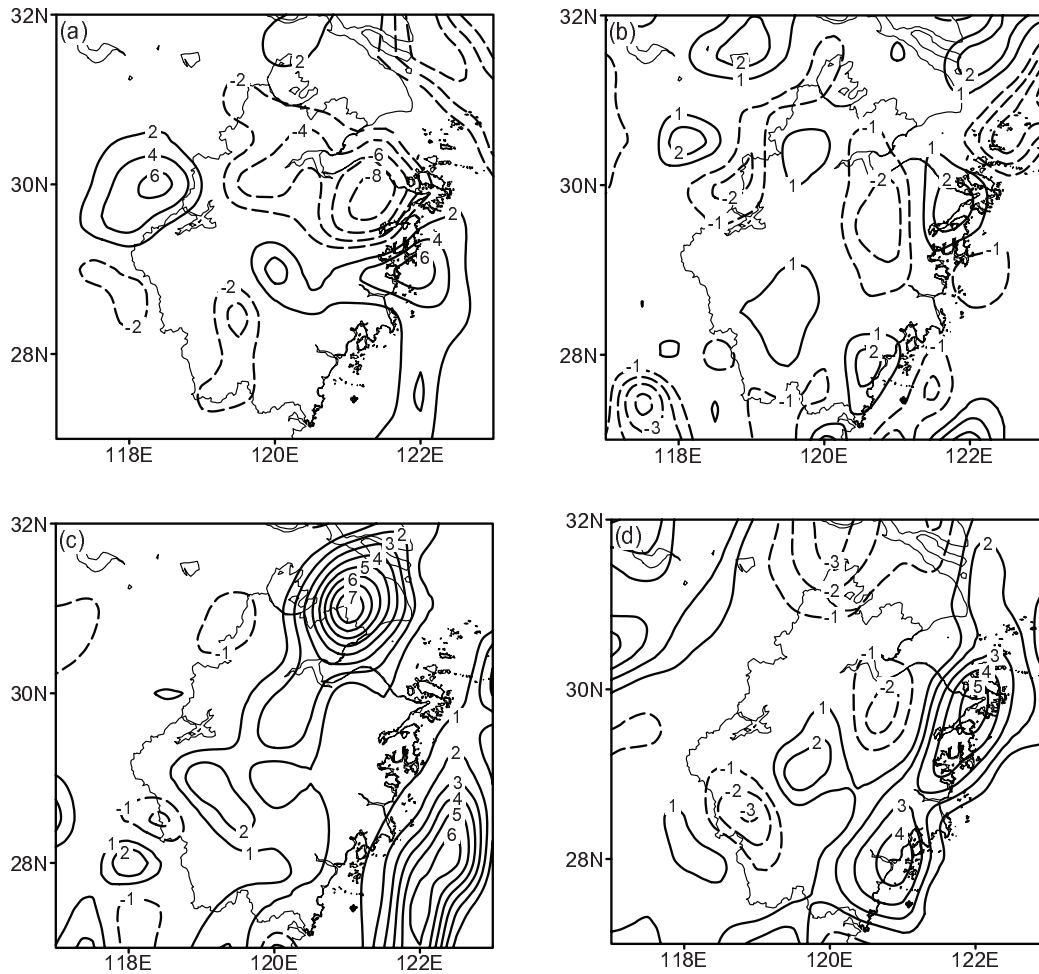


**Fig. 5.** The simulated 700-hPa quasi-geostrophic frontogenesis function analysis ( $\times 10^{-10}$   $\text{K m}^{-1} \text{s}^{-1}$ ) at (a) 1200 UTC 10, (b) 1800 UTC 10, (c) 0000 UTC 11 and (d) 0006 UTC 11 September 2010. The solid lines represent frontogenesis and the dashed lines represent frontolysis.

tion as follows:

$$\frac{d}{dt} |\nabla\theta| = -\frac{D}{2} |\nabla\theta| - \frac{1}{2|\nabla\theta|} \left[ E_{st} \left( \frac{\partial\theta}{\partial x} \right)^2 + 2E_{sh} \frac{\partial\theta}{\partial x} \frac{\partial\theta}{\partial y} - E_{st} \left( \frac{\partial\theta}{\partial y} \right)^2 \right], \quad (3)$$

where  $D = \frac{\partial u_g}{\partial x} + \frac{\partial v_g}{\partial y}$  is quasi-geostrophic divergence,  $E_{st} = \frac{\partial u_g}{\partial x} - \frac{\partial v_g}{\partial y}$  is quasi-geostrophic stretching deformation, and  $E_{sh} = \frac{\partial v_g}{\partial x} + \frac{\partial u_g}{\partial y}$  is quasi-geostrophic shear deformation. The first right-hand term in Eq. (3) is the divergence term and the second is the deformation term, which consists of stretching deformation and shear deformation.

The contribution of divergence and deformation

terms to the 750-hPa frontogenesis in the rainstorm area at 0000 UTC 11 September 2010 was examined. Figure 6a shows that more than 80% of the frontogenesis was caused by the deformation term. The distribution and magnitude of the positive deformation term corresponded well with the frontogenesis zone. Divergence also made some contribution to the frontogenesis, but was very small due to the weakness of the cold air. The maximum center of divergence term was only  $2.5 \times 10^{-10} \text{ K m}^{-1} \text{ s}^{-1}$ . Figures 6c and d provide the shear and stretching deformation terms. From these it can be seen clearly that, between the two deformation types, shear deformation made the greatest contribution to frontogenesis. On the contrary, stretching deformation was favorable for frontolysis. In other words, most frontogenesis resulted from shear deformation, which was caused by strong wind shear between weak northerly flow and strong

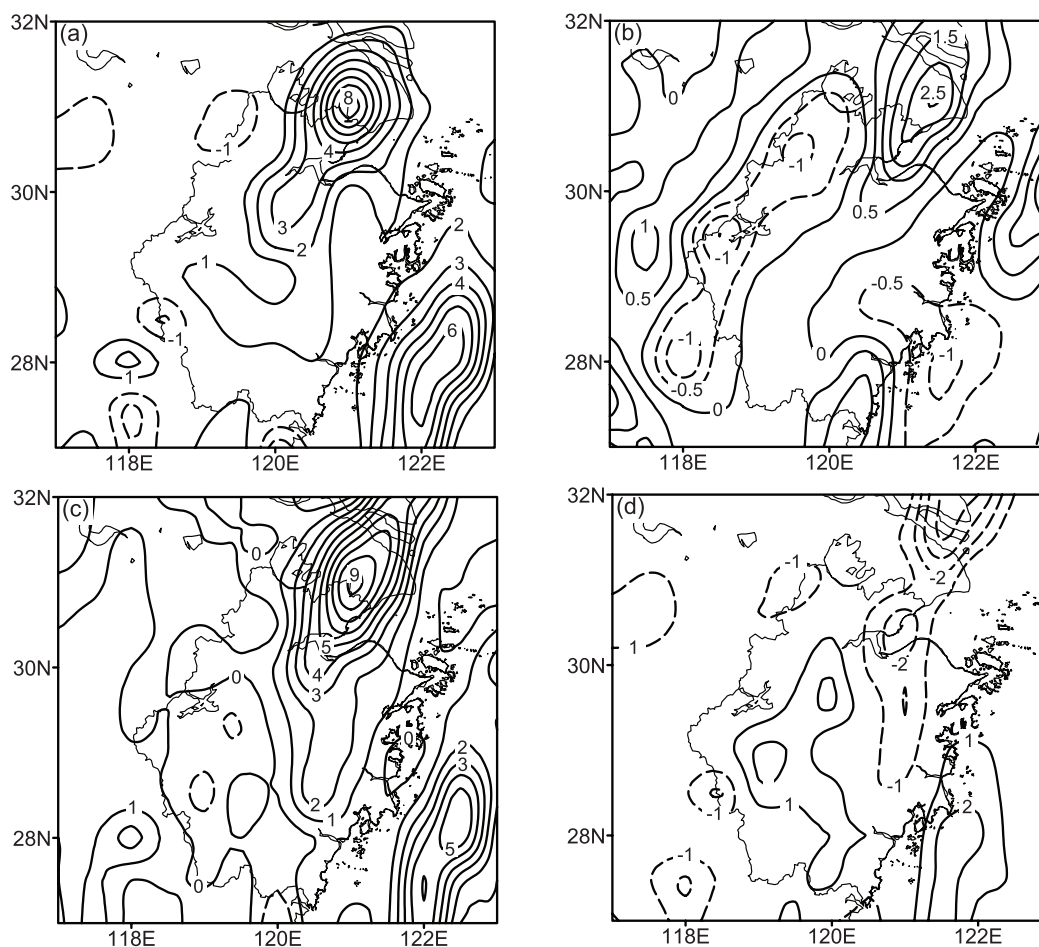


**Fig. 6.** The right-hand terms of the simulated 700-hPa quasi-geostrophic frontogenesis function ( $\times 10^{-10} \text{ K m}^{-1} \text{ s}^{-1}$ ) at 0000 UTC 11 September 2010: (a) deformation term, (b) divergence term, (c) shear deformation term, and (d) stretching deformation term. The solid lines represent the contribution to frontogenesis and the dashed lines represent the contribution to frontolysis.

southwesterly flow.

#### 4.2 Energy and atmospheric indices

A Skew- $T$  Log- $P$  diagram offers an instantaneous description of the atmosphere from the surface to about the 100-hPa level. Figure 7 displays the prevailing southwesterly jet throughout the whole troposphere at Baima Lake 12 hours before the rainstorm, which brought about plenty of moisture. The parcel lapse rate profile almost remained coincident with the dewpoint temperature profile from the surface to the tropopause, meaning that the whole layer had already been filled with moisture. So, the water vapor conditions for precipitation were suitable. At the same time, the parcel lapse rate profile remained on the right side of the environmental temperature profile below 175 hPa. The area inside these two profiles

implies that the convective available potential energy (CAPE) was sufficient for the supply to kinetic energy conversion, and the convective inhibiting energy (CIN) above 175 hPa was so small that it could be ignored. In fact, it could be accurately confirmed that CAPE was as large as 2385 J, but no CIN existed, from Table 1.

**Table 1.** Atmospheric index of Baima Lake Station at 0600 UTC 10 Sep 2010.

| Atmospheric Index |      |
|-------------------|------|
| CAPE (J)          | 2385 |
| CIN (J)           | 0    |
| LI                | -5   |
| K                 | 38   |
| TT                | 43   |

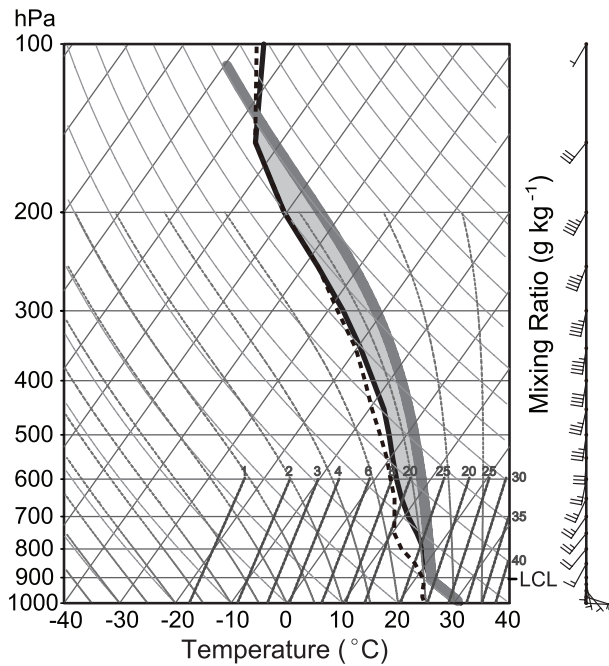


**Fig. 7.** Skew-*T* Log-*P* diagram of Baima Lake Station at 0600 UTC 10 September 2010. The data come from the NCEP grib2 dataset. The black bold profile gives environmental sounding (°C). The black dashed profile represents vertical dewpoint temperature of environment (°C). The dark gray bold profile stands for the parcel lapse rate (°C). The light gray shadowing represents CAPE (J). The wind barb vectors are at full barb of 5 m s<sup>-1</sup>.

According to the definition of free convection level (FCL), FCL can be affirmed at a height below 900 hPa from Fig. 7, which means that convection could easily be triggered, and would develop dramatically under favorable convection indexes given in Table 1. The Lifted Index (LI), *K*-index and Total-Totals index (TT) all satisfied the local empirical threshold for strong convective weather.

### 4.3 Stratification and omega equation

The low-level southwesterly jet on the western margin of the Western Pacific Subtropical High not only brought about plenty of moisture, but also heat. Four hours before the rainstorm, there was strong positive horizontal advection of equivalent potential temperature at 850 hPa. The positive center was located near Baima Lake, with an intensity of  $79.3 \times 10^{-5} \text{ K s}^{-1}$  (Fig. 8a). At the upper level of 200 hPa, there was weak negative horizontal advection coinciding with the positive advection vertically. The negative center was about  $-10.2 \times 10^{-5} \text{ K s}^{-1}$  and transported weak dry cold air to the upper level of northern Zhejiang (Fig. 8b). The negative and positive advection centers made the weak cold dry air flow over the strong warm moist air, contributing to convectively unstable stratification.

According to Holton (2004), the omega equation can be expressed as:

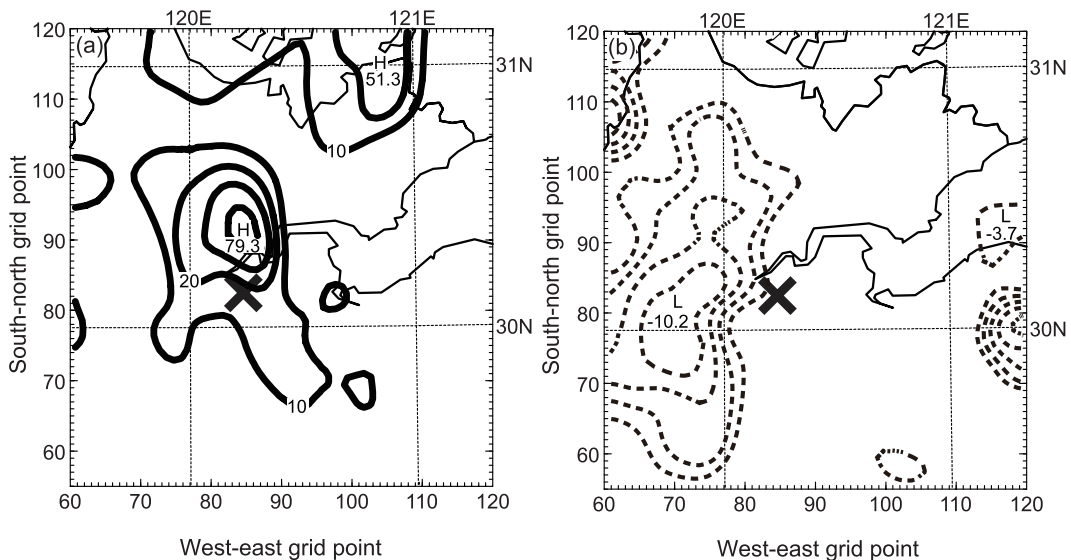


**Fig. 8.** Simulated horizontal advection of equivalent potential temperature of D04 at 2010 UTC 10 September 2010. (a) The 850-hPa positive horizontal advection of equivalent potential temperature (solid lines, contour interval of  $10 \times 10^{-5} \text{ K s}^{-1}$ ). (b) The 200-hPa negative horizontal advection of equivalent potential temperature (dashed lines, contour interval of  $-2 \times 10^{-5} \text{ K s}^{-1}$ ). The black cross represents the location of Baima Lake, where the simulated maximum rainfall center of D04 was also located.

$$\left(\nabla^2 + \frac{f_0^2}{\sigma} \frac{\partial^2}{\partial p^2}\right) \omega = \frac{f_0}{\sigma} \frac{\partial}{\partial p} \left[ \mathbf{V}_g \cdot \nabla \left( \frac{1}{f_0} \nabla^2 \Phi + f \right) \right] + \frac{1}{\sigma} \nabla^2 \left[ \mathbf{V}_g \cdot \nabla \left( -\frac{\partial \Phi}{\partial p} \right) \right] - \frac{\kappa}{\sigma p} \nabla^2 J, \quad (4)$$

where  $\omega \equiv dp/dt$  is the pressure change following the motion;

$$\sigma \equiv -RT_0 p^{-1} d \ln \theta_0 / dp$$

and  $\theta_0$  is the potential temperature corresponding to the basic state temperature  $T_0$ ;  $f$  is the Coriolis parameter;  $f_0 = 2\Omega \cos 45^\circ$ ;  $\Phi$  is geopotential height and  $\Phi = gz$ ; and  $\kappa = R/c_p$ ;

$$J = c_p \left( \frac{\partial T}{\partial t} + u \frac{\partial T}{\partial x} + v \frac{\partial T}{\partial y} + \omega \frac{\partial T}{\partial p} \right) - \alpha \omega$$

is the first law of thermodynamics and  $\alpha$  is specific volume.

The right-hand side in Eq. (4) can be expressed approximately as

$$\left(\nabla^2 + \frac{f_0^2}{\sigma} \frac{\partial^2}{\partial p^2}\right) \omega \approx \frac{f_0}{\sigma} \left[ \frac{\partial \mathbf{V}_g}{\partial p} \cdot \nabla \left( \frac{1}{f_0} \nabla^2 \Phi + f \right) \right], \quad (5)$$

and the left-hand term in Eq. (4) is approximately as follows

$$\left(\nabla^2 + \frac{f_0^2}{\sigma} \frac{\partial^2}{\partial p^2}\right) \omega \approx - \left[ k^2 + l^2 + \frac{1}{\sigma} \left( \frac{f_0 \pi}{p_0} \right)^2 \right] \omega, \quad (6)$$

where  $k$  and  $l$  are the wave numbers in the  $x$  and  $y$  directions. It shows that the left-hand side of Eq. (4) is proportional to  $-\omega$ .  $\omega < 0$  implies upward vertical motion and is proportional to vertical velocity. The right-hand side of Eq. (5) represents the advection of absolute vorticity by thermal wind. Thus, upward motion is forced where the right-hand side of Eq. (5) is positive and downward motion is forced where it is negative.

The 850-hPa results calculated by the right-hand side of Eq. (5) at 1100 UTC 11 September 2010 (Fig. 9) shows that there was positive advection of absolute vorticity by thermal wind from mid-west to northeast Zhejiang. The maximum center was about  $0.6 \times 10^{-10} \text{ Pa s}^{-1} \text{ m}^{-1}$  and located to the south of the Qiantang River estuary near Baima Lake. The positive vorticity is associated with negative geopotential deviations, as vorticity is proportional to the Laplacian of geopotential, and thus positive advection of absolute vorticity

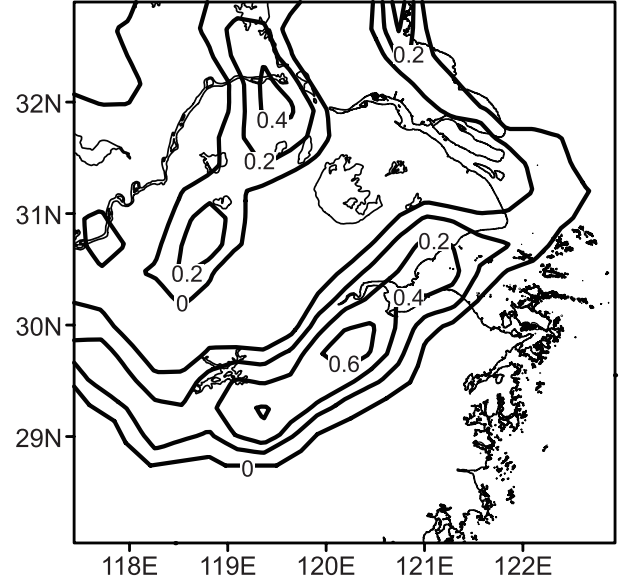


**Fig. 9.** Simulated 850-hPa omega equation diagnosis ( $\times 10^{-10} \text{ Pa s}^{-1} \text{ m}^{-1}$ ) at 1100 UTC 11 September 2010. The area with positive values means there is upward movement.

by thermal wind implies a falling geopotential (Holton, 2004). Since there was low-level warm-air advection (Fig. 8a), the only way to cool the atmosphere as required by the thickness tendency was by adiabatic cooling through upward vertical motion. Thus, the low-level warm-air advection played an important role too in producing and intensifying updrafts.

## 5. The structure of remnant clouds

### 5.1 Temperature of black-body intensity

The remnant clouds were responsible for the rainstorm. Before the rain started (Fig. 10a), the remnant clouds were very weak and small, and the temperature of black-body (TBB) intensity was only about  $-50^\circ\text{C}$ . However, the remnant clouds suddenly strengthened when moved northeastward to the Hangzhou area three hours later (Fig. 10b), their area expanded rapidly, and the maximum TBB center located at Baima Lake almost reached  $-70^\circ\text{C}$ . At the time, the rainfall peak with one-hour precipitation of 102.3 mm appeared at the same place (Fig. 2b). Then, the remnant clouds kept extending northeastward to the Jiaxing area in the next few hours. During that time, they split out into more cloud clusters toward the northeast, taking the rain band there too (Fig. 10c). Finally, after the remnant clouds left Zhejiang Province, the rainfall ended very soon (Fig. 10d). The period of time from 2200 UTC 10 to 0200 UTC 11 September 2010 was

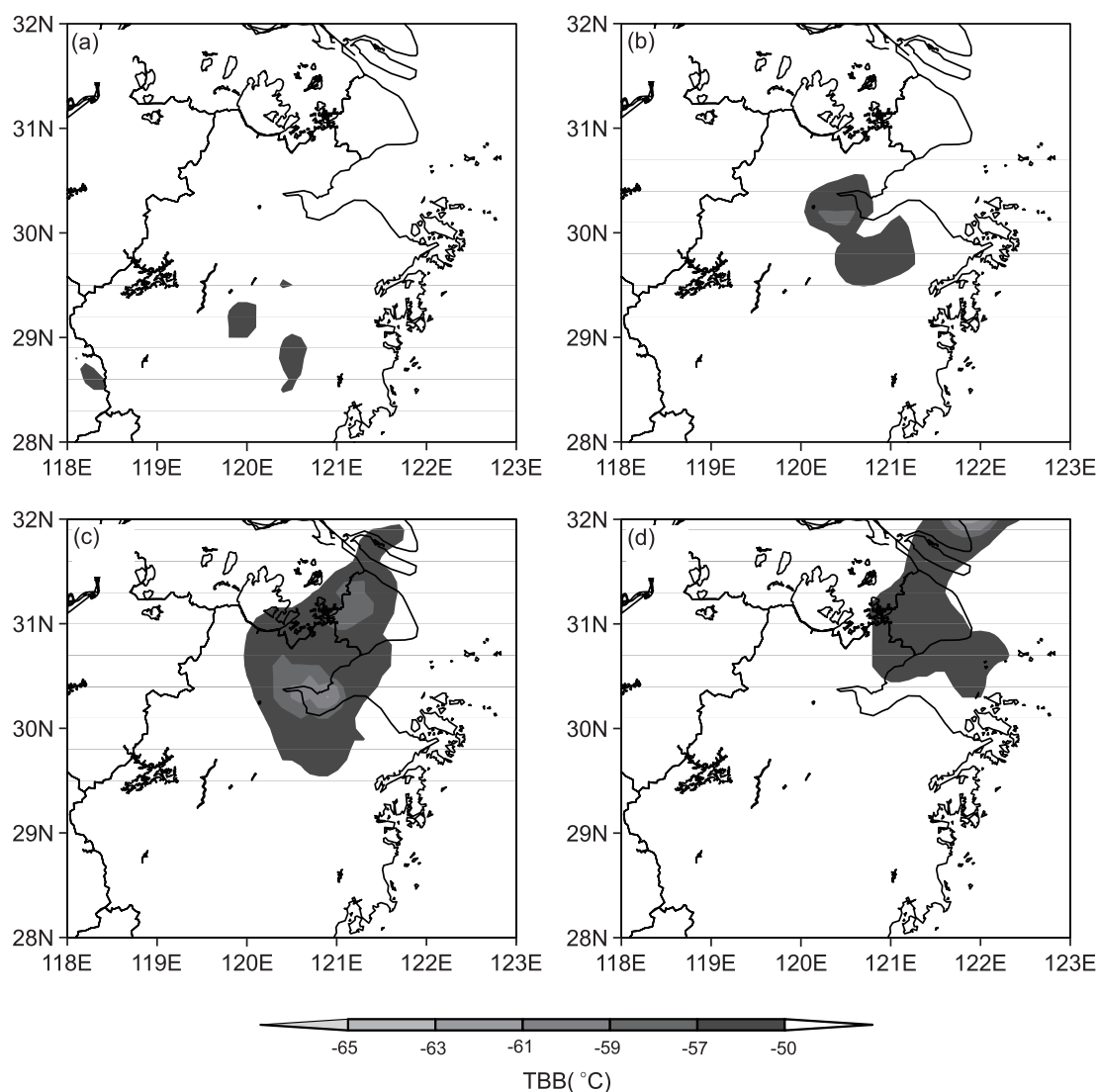


**Fig. 10.** TBB from FY2D satellite data (gray shadows are the areas where TBB is stronger than  $-50^{\circ}\text{C}$ ) at (a) 2000 UTC 10, (b) 2300 UTC 10, (c) 0300 UTC 11, (d) 0600 UTC 11 September 2010.

very crucial. During that time, the remnant clouds went through sudden reinforcement and the heaviest rainfall occurred.

### 5.2 Doppler radar reflectivity

Doppler radar reflectivity at 1 km in Hangzhou was recorded during the crucial period to further examine the detailed inner structure of the remnant clouds. First there was a microscale convective cell generated near Baima Lake on the north side of the remnant clouds (Fig. 11a). Then, as the remnant clouds moved on, more convective cloud cells formed one-by-one in a line (Fig. 11b). The area of radar echo larger than 40 dBZ in the convective line stretching from southwest to northeast was about 200 km long, belong-

ing to the meso- $\beta$  scale. Furthermore, as the remnant clouds intensified, the circulation became tighter and more cyclonic. A distinct “eye zone” to the east side of the meso- $\beta$  scale convective line subsequently formed, just like that in a typhoon center (Figs. 11c and d). A cross section along the meso- $\beta$  scale convective line (Fig. 11e) shows that the convective clusters were strong and active. Their reflectivity exceeded 45 dBZ and extended from the surface to 6 km high. In fact, there were multiple microscale convective cells of tens of kilometers long imbedding in the convective line. Figure 11f displays simulated maximum reflectivity at the 1-km level. Although the structure of the simulated remnant clouds was not as tight as the observed TD, the simulated echo band was quite close

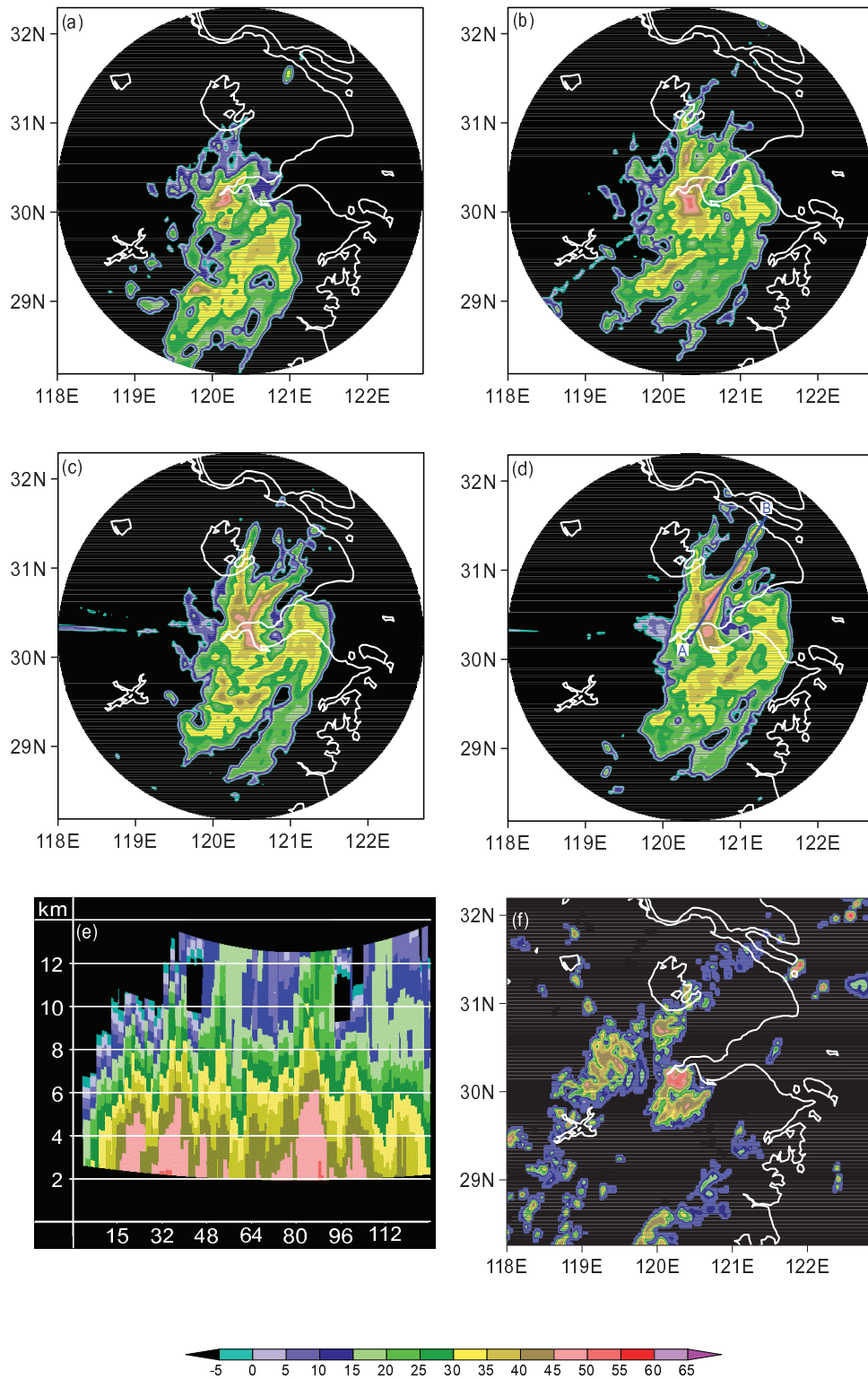


**Fig. 11.** Doppler radar reflectivity (contour interval of 5 dBZ) at 1-km high in Hangzhou at (a) 2200 UTC 10, (b) 0018 UTC 11, (c) 0116 UTC 11, (d) 0200 UTC 11 September 2010, and (e) cross section along the meso- $\beta$  scale convective line in Fig. 11d. (f) Simulated maximum reflectivity at 1-km high at 0130 UTC 11 September 2010. The blue line in Fig. 11d is the cross line of Fig. 11e.

to observation, which increases the credibility of the simulated results. Furthermore, the simulated results can be used to investigate the physical mechanisms of the genesis and development of MCSs.

## 6. Moist potential vorticity

### 6.1 Slantwise vorticity development theory

Wu et al. (1995) proposed a theory of slantwise vorticity development (SVD) based on the  $Z$ - and  $P$ -coordinates from the moist isentropic potential vorticity development theory. In the  $P$ -coordinate system, assuming that the horizontal variation of vertical velocity is much smaller than the vertical shear of horizontal velocity, the moist potential vorticity (MPV) equation can be expressed as

$$P_m = -g(\mathbf{f}\mathbf{k} + \nabla_p \times \mathbf{v}) \cdot \nabla_p \theta_e, \quad (7)$$

where  $\theta_e$  is the equivalent potential temperature,  $\mathbf{v}$  is horizontal wind vector, and  $f$  is the Coriolis parameter. If the first term on the right-hand side of Eq. (7) is defined as the vertical component, and the second term is defined as the horizontal component, then Eq. (7) can be written as:  $P_m = P_{m1} + P_{m2}$ , and

$$\begin{cases} P_{m1} = -g\zeta_p \frac{\partial \theta_e}{\partial p} \\ P_{m2} = -g\mathbf{k} \times \frac{\partial \mathbf{v}}{\partial p} \cdot \nabla_p \theta_e \end{cases}, \quad (8)$$

where

$$\zeta_p = f + \left( \frac{\partial v}{\partial x} - \frac{\partial u}{\partial y} \right)_p,$$

is the absolute vorticity in the  $P$ -coordinate system. Then, the conservation of MPV results in

$$P_m = P_{m1} + P_{m2} = \alpha \zeta_\theta |\nabla \theta_e|, \quad (9)$$

where  $\zeta_\theta$  is the vertical projection of absolute vorticity.  $P_{m2}$  is usually referred to as the moist baroclinic term for containing the vertical shear of horizontal wind and horizontal gradient of equivalent potential temperature. Correspondingly,  $P_{m1}$  is known as the moist barotropic term.

Wu et al. (1995) deduced that MPV is approximately conserved in a saturated atmosphere without diabatic heating and frictional dissipation and then used this property to investigate the development of vertical vorticity in moist baroclinic processes. The results showed that whether the atmosphere is symmetrically moist (stable or unstable), or convectively stable or unstable, so long as the moist isentropic surface is slantwise, the reduction of convective stability or instability and the increase of the vertical shear of horizontal wind or moist baroclinicity can result in the increase of vertical vorticity. The larger the decline of the moist isentropes is, the more vigorous the development of vertical vorticity will be. This is known as SVD theory, and SVD theory is very useful for analysis of the genesis of mesoscale weather phenomena, such as rainstorms (Duan and Li, 2000; Li and Shou, 2000; Shou et al., 2001).

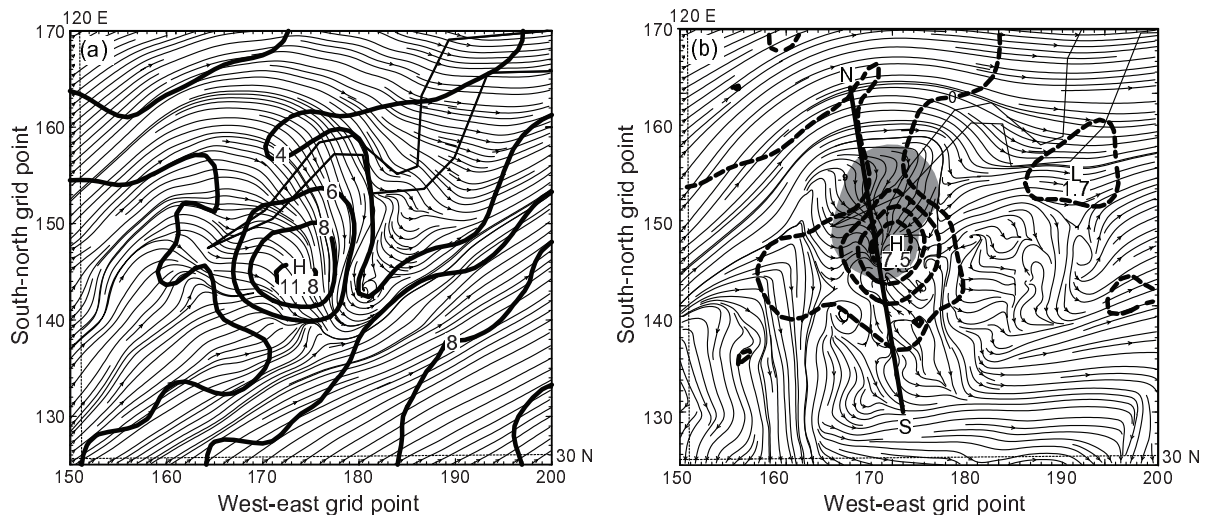


**Fig. 12.** Simulated stream fields of D04 at 0055 UTC 11 September 2010. (a) The 850-hPa stream field (thin lines with arrows) and horizontal wind velocity (thick line, contour interval of  $2 \text{ m s}^{-1}$ ). (b) The 350-K moist isentropic surface stream field (thin lines with arrows), the 750-hPa MPV (dashed lines, contour interval of  $2 \times 10^{-6} \text{ m}^{-2} \text{ K s}^{-1} \text{ kg}^{-1}$ ), and area of past 1-hour's rainfall larger than 50 mm (dark gray shadow). The thick line S-N represents the cross section of Fig. 13.

## 6.2 MPV analysis of the MCSs

Although MPV was not conserved in the rainstorm process in this study, which involved diabatic heating and frictional dissipation, SVD theory can still be used to analyze the genesis and development mechanisms of the mesoscale systems in the rainstorm. Figure 12a shows the 850-hPa stream field at rainfall peak time. The southwesterly flow was invaded by a northerly jet travelling downward from upper air. The maximum velocity of the jet was about  $12 \text{ m s}^{-1}$ , and the jet center was located just right above the rainstorm area. On the moist isentropic surface of  $\theta_e = 350 \text{ K}$

(Fig. 12b), there was distinct convergence from flows around the rainstorm area. Corresponding to the rainstorm area, a positive anomaly of MPV appeared at 750 hPa, with a maximum intensity of about  $7.5 \times 10^{-6} \text{ m}^{-2} \text{ K s}^{-1} \text{ kg}^{-1}$ . Under the effect of convergence and positive MPV anomaly, there was a microscale cyclonic vortex generated in the rainstorm area. Comparing Fig. 12 with Fig. 11, it can be deduced that the vortex was one of the microscale convective cells appearing on the west side of the “eye zone” of the remnant clouds at 2200 UTC 10 September 2012, if considering the time lag between simulation results and observation.

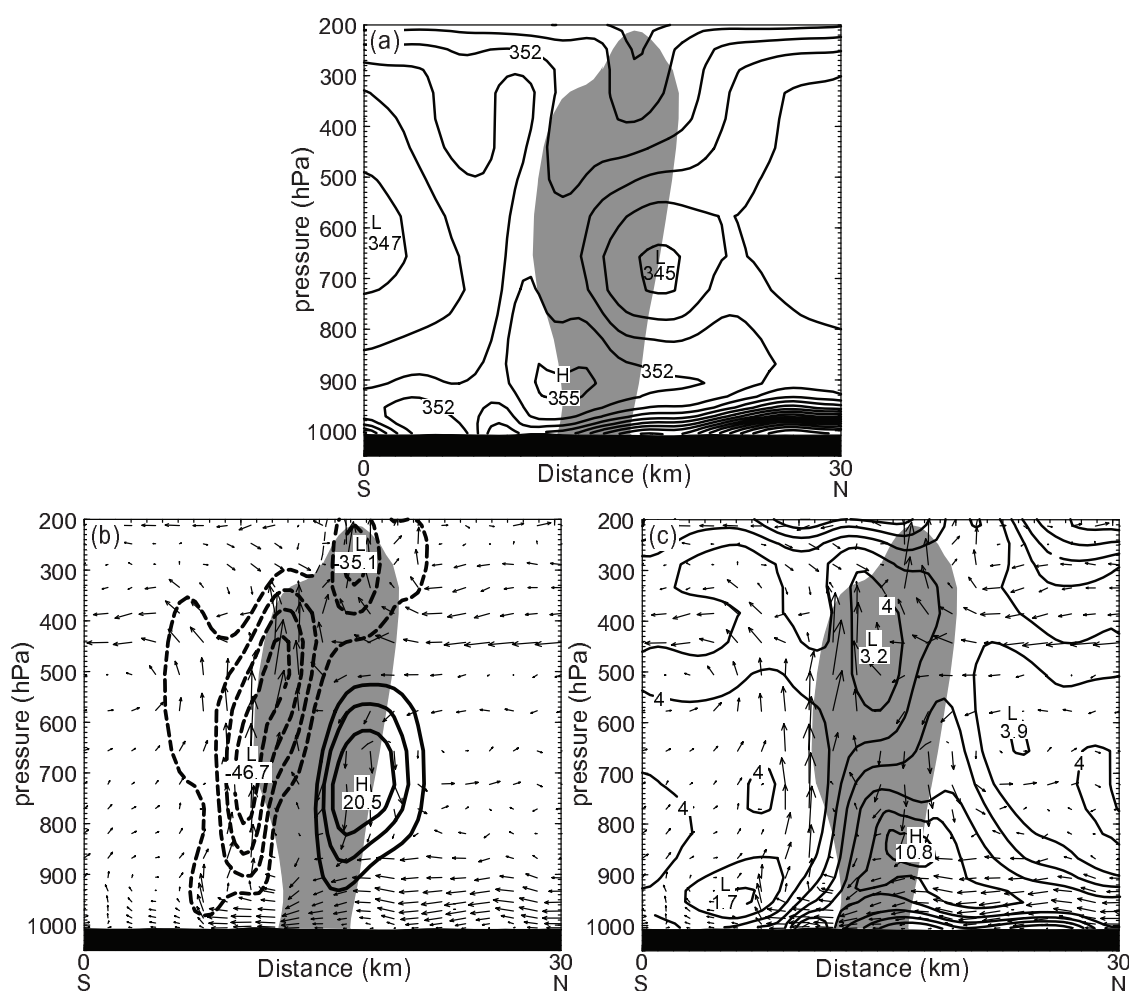


**Fig. 13.** Simulated cross section through the rainfall center, vortex center and positive MPV anomaly center of D04 at 0055 UTC 11 September 2010. (a) Equivalent potential temperature (thick lines, contour interval of 2 K). (b) Positive vertical velocity greater than  $5 \times 10^{-2} \text{ hPa s}^{-1}$  (solid line, contour interval of  $5 \times 10^{-2} \text{ hPa s}^{-1}$ ), negative vertical velocity less than  $-10 \times 10^{-2} \text{ hPa s}^{-1}$  (dashed lines, contour interval of  $-10 \times 10^{-2} \text{ hPa s}^{-1}$ ). (c) Horizontal wind velocity (solid lines, contour interval of  $1 \text{ m s}^{-1}$ ). The dark gray shadow is the total area of the cloud ice mixing ratio, cloud water mixing ratio and rain water mixing ratio greater than  $4 \text{ g kg}^{-1}$ , representing the microscale convective cell. The arrows in Fig. 11a and 10c are wind circulation vectors at the full vector of  $10 \text{ m s}^{-1}$ . The cross line can be seen in Fig. 11b.

In order to further understand the genesis and development mechanisms of the MCSs, a south–north cross section was made through the rainfall center, vortex center and positive MPV anomaly center at the same time (Fig. 13). One of the microscale convective cells constituting a MCS is represented by the area of dark gray shadow where the total of cloud ice mixing ratio, cloud water mixing ratio and rain water mixing ratio was larger than  $4 \text{ g kg}^{-1}$ . The microscale convective cell was developing intensively. Its vertical structure was very deep, stretching from surface to tropopause.

Figure 13a shows that, on the south side of the microscale convective cell, the warm moist flow with maximum equivalent potential temperature of 355 K was very active in the lower levels and the air was convectively unstable. On the north side, a cold dry flow from the north travelled southward near the surface, whose central equivalent potential temperature was 330 K below. At the meeting area of these two flows with opposite natures, the gradient of equivalent potential temperature was quite steep. The microscale convective cell formed at the southern edge of the gradient area. As the cold dry flow kept moving southward near the surface below 950 hPa, the warm moist air was lifted upward and kept moving northward along the top of the cold dry flow at about 900 hPa. On the one hand, the warm moist air arriving at the north side of the microscale convective cell made the atmosphere there convectively unstable too, because the air above 900 hPa on the north side was colder and drier. On the other hand, the unstable air on the south side of the microscale convective cell ascended intensely after the initial uplift. The maximum velocity of the updraft reached  $-46.7 \times 10^{-2} \text{ hPa s}^{-1}$  (Fig. 13b). Strong ascending air brought plenty of heat and moisture to the middle and upper levels, leading to a significant incline of the isentropic surface. The equivalent potential temperature surface in the middle level near the microscale convective cell was almost perpendicular to the ground, so the atmosphere in this area was approximately convectively neutral ( $\partial\theta_e/\partial p \approx 0$ ) (Fig. 13a). Therefore, when air from the south and north flowed into the rainstorm area, the convective instability would reduce, which was favorable for the intensification of cyclonic vorticity and the genesis of a MCS according to SVD. In return, the MCS genesis and rainstorm would release a lot of latent heat, which would keep the isentropic surface inclining for a period to further the development of the MCS.

As previously mentioned, the vertical shear of horizontal wind can also increase vertical vorticity. Figure 13c displays a significant difference in horizontal

wind velocity between lower and upper levels in a microscale convective cell. The maximum velocity of the northerly jet at 850 hPa was about  $10.8 \text{ m s}^{-1}$ , but the wind velocity above was only  $3\text{--}4 \text{ m s}^{-1}$ . That is to say, the vertical shear of horizontal wind and the gradient of equivalent potential temperature both intensified when the cold dry air from the north ran into the warm moist air from the south. These represent another two advantages for the genesis and development of cyclonic vorticity and MCSs.

### 6.3 MPV evolution

Figure 12b shows that there was a positive anomaly of MPV at 750 hPa in the rainstorm area. So, the variation of rainstorm-area mean MPV,  $P_{m1}$  and  $P_{m2}$  with time at 750 hPa is given in Figs. 14a–c to understand the evolution of MPV and analyze the contribution of  $P_{m1}$  and  $P_{m2}$  made at each stage.

According to Fig. 14a, MPV did not turn positive until 0030 UTC 11 September 2010, and there were several positive peaks and troughs in MPV curves from 0030 UTC to 0120 UTC 11 September 2010. The sequential occurrence of peaks implies the continuous genesis and development of microscale convective cells embedding in the MCS. Furthermore, the maximum peak of MPV of  $0.4 \text{ PVU}$  ( $\text{PVU} = 10^{-6} \text{ m}^{-2} \text{ K s}^{-1} \text{ kg}^{-1}$ ) appeared at 0055 UTC 11 September 2010, when the heaviest simulated rainfall occurred.

Comparing Figs. 14a–c, the first appearance of the positive peak of  $P_{m2}$  was at about 0015 UTC 11 September 2010, which was earlier than that of MPV and  $P_{m1}$ . According to Eq. (8),  $P_{m2}$  is closely related to the horizontal gradient of equivalent potential temperature, and the timing of the  $P_{m2}$  peak corresponded well to the sudden strengthening of the horizontal gradient of equivalent potential temperature (Fig. 14f), which was caused by frontogenesis in the lower levels. The evolution of  $P_{m1}$  was similar to that of MPV. It was nearly always negative except for the time between 0040 UTC and 0130 UTC 11 September 2010 (Fig. 14b). Equation (8) shows that  $P_{m1}$  is the moist barotropic term and in most cases the vertical gradient of the equivalent potential temperature determines the value of  $P_{m1}$ . It can be seen from Fig. 14e that the air in the rainstorm area was first convectively unstable on average, at the beginning of rainfall, and the vertical gradient of the equivalent potential temperature was about as large as  $0.3 \times 10^{-3} \text{ K Pa}^{-1}$ . Then, the convective instability rapidly decreased to  $0.075 \times 10^{-3} \text{ K Pa}^{-1}$  in less than one hour at 0055 UTC 11 September 2010. According to SVD theory, the reduction of convective instability would result in an intense increase of vertical vorticity (Fig.

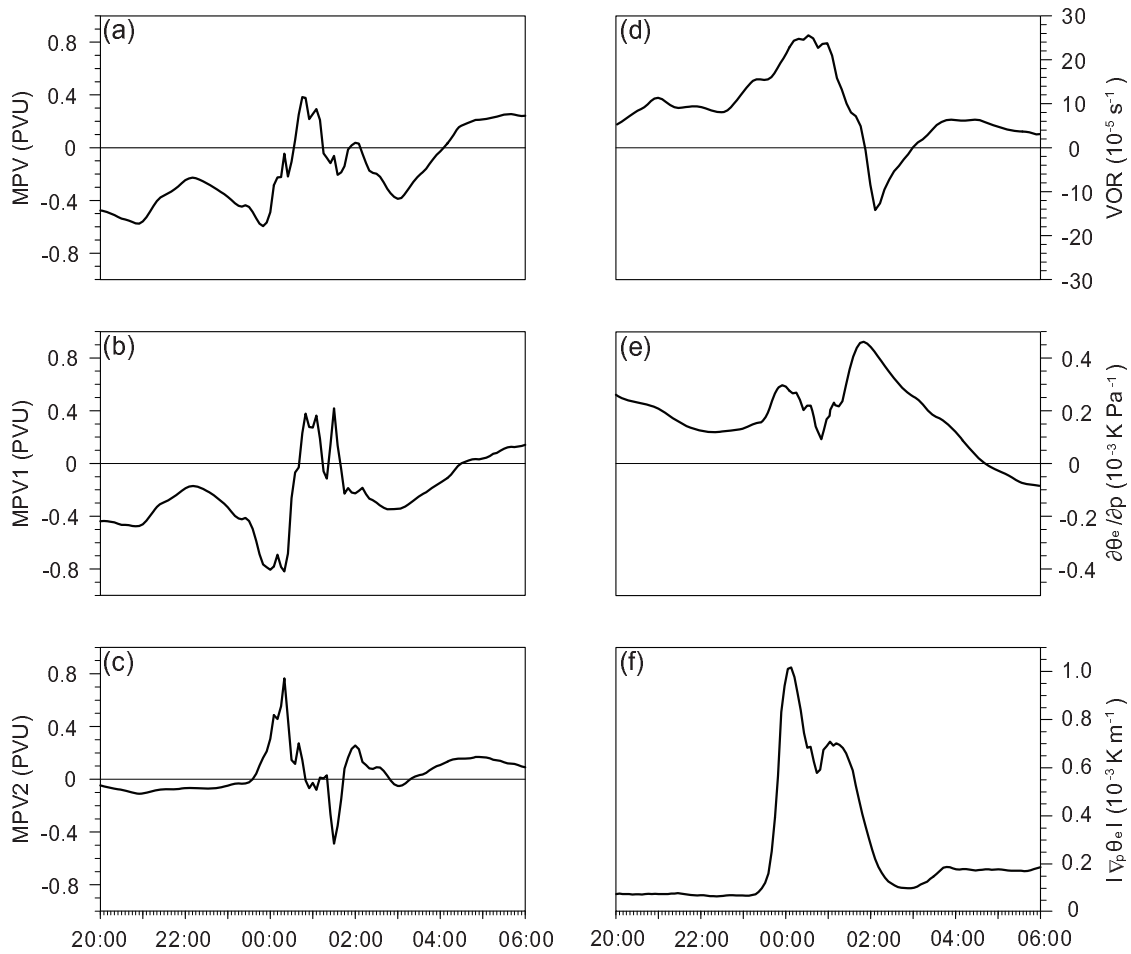


**Fig. 14.** Variation of rainstorm-area mean (a) MPV (units of PVU =  $10^{-6} \text{ m}^{-2} \text{ K s}^{-1} \text{ kg}^{-1}$ ), (b) MPV1 (units of PVU), (c) MPV2 (units of PVU), (d) relative vertical vorticity (units of  $10^{-5} \text{ s}^{-1}$ ), (e) vertical gradient of equivalent potential temperature (units of  $10^{-3} \text{ K Pa}^{-1}$ ), and (f) horizontal gradient of equivalent potential temperature (units of  $10^{-3} \text{ K m}^{-1}$ ) with time at 750 hPa.

14d), and the intense strengthening of vertical vorticity would then contribute to the development of MCSs and produce heavy rainfall in a short period of time.

#### 6.4 Conditional symmetric instability evaluation

Figure 14a shows negative MPV at 750 hPa before 0030 UTC 11 September 2010, which indicates the possible occurrence of conditional symmetric instability (CSI). CSI is usually evaluated by equivalent potential vorticity (EPV) in a purely meridional wind flow in thermal wind balance, and EPV can be expressed as:

$$\text{EPV} = g \left[ \left( \frac{\partial M_g}{\partial p} \frac{\partial \theta_e}{\partial x} \right) - \left( \frac{\partial M_g}{\partial x} \frac{\partial \theta_e}{\partial p} \right) \right], \quad (10)$$

where  $M_g = V_g + fx$ , is referred to as absolute momentum;  $V_g$  is the horizontal geostrophic wind component,

normal to the cross section; and  $x$  is the distance from the left end of the cross line and increases toward the warm air (Emanuel, 1983, 1988). The necessary conditions for CSI are that the lifted parcel is saturated and the slope of the  $M_g$  surface is shallower than the slope of the  $\theta_e$  surface or, equivalently,  $M_g$  decreases in the positive  $x$  direction along a  $\theta_e$  surface (Sanders and Bosart, 1985).

To simplify the mathematics and to best comprehend the physical mechanisms important to slantwise convection, in this study, CSI was evaluated by a vertical cross section of absolute momentum and equivalent potential temperature perpendicular to the thermal wind and crossing through the rainfall center. Figure 15a gives the 850-hPa geopotential height at 1500 UTC 11 September 2010. The cross line A–B is perpendicular to the isopleths of the geopotential difference between 850 hPa and 500 hPa (data not shown).

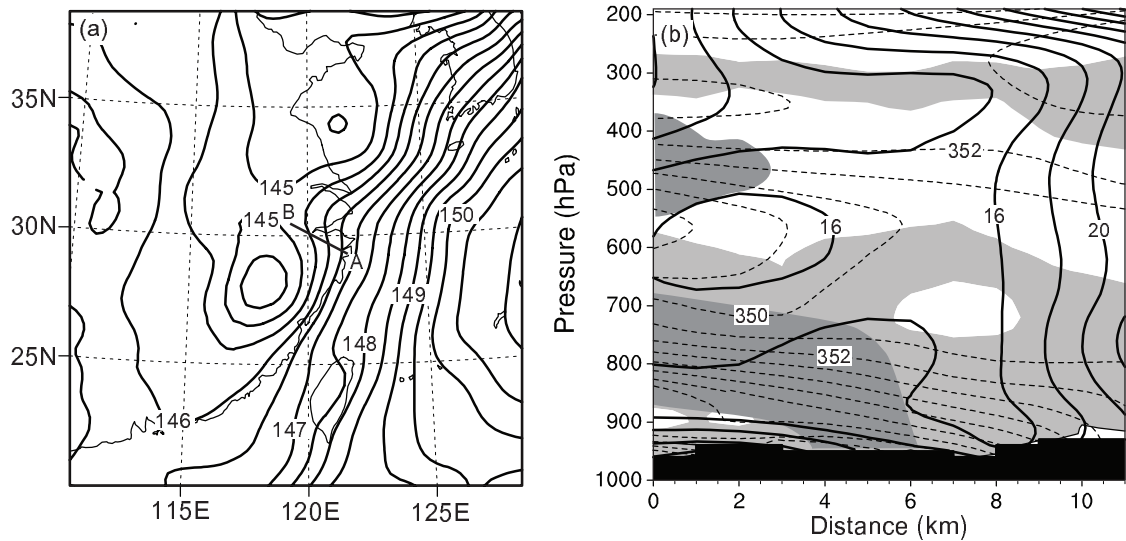


**Fig. 15.** (a) Simulated 850-hPa geopotential height (contour interval of 0.5 gpm) at 1500 UTC 10 September 2010. The line A–B represents the cross line of Fig. 15b. (b) Vertical cross section of quasi-geostrophic absolute momentum (solid lines, contour interval of  $2 \text{ m s}^{-1}$ ) and equivalent potential temperature (dashed lines, contour interval of 1 K). The dark shaded represents the CSI area, and the light shaded area represents the convectively unstable area.

Since thermal wind blows along the isopleths of the geopotential difference field, the cross line is perpendicular to the thermal wind too, and the direction of the cross line is toward the warm air. Both  $M_g$  and  $\theta_e$  along the cross section are analyzed in Fig. 15b.

Owing to the low-level southwesterly jet, the air was warmer and moister than that in the middle and upper levels, which made the stratification below 600 hPa convective unstable (light shading in Fig. 15b). Moreover, the low-level southwesterly jet increased the flow into the cross section, leading the  $M_g$  surface below 600 hPa to tilt to the left. The tilting angle got so large that the  $M_g$  surface is nearly horizontal within about 8 km from the left end of the cross section, because the center of the low-level southwesterly jet was closer to the left end and the flow into the cross section got stronger there. Hence, the area bounded from 900 to 700 hPa, and from about 2 km to the cross section center appears to have the  $M_g$  decreasing in the positive  $x$  direction along  $\theta_e$  surface (dark shaded area in Fig. 15b), indicating the necessary criterion for CSI is satisfied. The convectively unstable area was included in the CSI area, but vertical convection was more advantageous than slantwise convection, because vertical convection increases faster than slantwise convection. There was another CSI area on the left-hand side of the cross section between 450 to 550 hPa. However, it was shallow and at the upper level, low humidity and weak vertical movement did little to contribute to the

development of the storm. Thus, the redevelopment of the storm was mainly caused by low-level vertical convection triggered by frontogenetical forcing.

## 7. Kinetic energy analysis

Palmen (1958) proposed that the conversion between potential energy and kinetic energy as well as the conversion of latent heat are the energy sources for the maintenance of TCs and their associated rainstorms. Li et al. (2005) calculated the kinetic energy budgets for typhoons dissipating quickly within 12 hours after landfall (referred to as STCs) and typhoons sustaining for a long period (3–5 days) after landfall (referred to as LTCs) on the basis of dynamic composite analysis. Their findings showed that the kinetic energy in the lower layers increases for LTCs owing to the convergence of kinetic energy flux, which would partly compensate consumption as a result of friction. In the upper levels, LTCs draw kinetic energy in the period 36–60 hours after landfall due to baroclinic and subgrid-scale kinetic energy generation. The kinetic energy of STCs is only dissipated without compensation. Li and Shou (1995) computed the kinetic energy balance and distribution for a landed typhoon decaying quickly and maintaining for a long period before disintegration. The results showed that short-lived storms are related to the horizontal flux divergence of upper-troposphere kinetic energy and the

crossing-isobaric motion, whereas long-lived storms receive inputs of kinetic or potential energy from the ambient atmosphere. Therefore, in the present work, the kinetic budget for the area of the rainstorm lasting for six hours was calculated and analyzed to find out

the energy sources for the sudden reinforcement of the rainfall.

According to the computing method of Lin and Coover (1988), the kinetic energy equation for a non-hydrostatic system can be written as:

$$\begin{aligned}
 \frac{1}{\sigma} \iint \frac{\partial \bar{\rho} K_3}{\partial t} d\sigma &= -\frac{1}{\sigma} \iint \nabla_2 \cdot (\bar{\rho} K_3 \mathbf{V}_2) d\sigma - \frac{1}{\sigma} \iint \frac{\partial \bar{\rho} K_3 w}{\partial z} d\sigma - \frac{1}{\sigma} \iint \mathbf{V}_2 \cdot \nabla_2 p' d\sigma - \frac{1}{\sigma} \iint w \frac{\partial p'}{\partial z} d\sigma + \\
 &\quad \text{LTK} \qquad \qquad \text{HFD} \qquad \qquad \text{VFD} \qquad \qquad \text{HGE} \qquad \qquad \text{VGE} \\
 &\quad \frac{1}{\sigma} \iint \bar{\rho} g w \left( \frac{T'_v}{T_v} - q_r \right) d\sigma + \frac{1}{\sigma} \iint \bar{\rho} \mathbf{V} \cdot \mathbf{F} d\sigma, \\
 &\quad \qquad \qquad \text{BUP} \qquad \qquad \qquad \text{FDI}
 \end{aligned} \tag{11}$$

where  $\sigma$  is the area of the rainstorm;

$$K_3 = \frac{1}{2}(u^2 + v^2 + w^2)$$

is the total kinetic energy per unit mass;  $\mathbf{V}_2 = u\mathbf{i} + v\mathbf{j}$  is the horizontal wind vector, and  $\mathbf{V} = u\mathbf{i} + v\mathbf{j} + w\mathbf{k}$  is the three-dimensional wind vector;

$$\nabla_2 = \frac{\partial}{\partial x} \mathbf{i} + \frac{\partial}{\partial y} \mathbf{j}$$

is the horizontal gradient vector;  $\mathbf{F} = F_x\mathbf{i} + F_y\mathbf{j}$  is the friction vector;  $\bar{T}_v$  is the environmental mean virtual temperature and  $T'_v$  is the virtual temperature deviation from the environmental mean;  $\bar{\rho}$  is the environmental mean atmospheric density and  $p'$  represents the deviation from the environmental mean. The term on the left-hand side of Eq. (11) represents local variation of kinetic energy with time (LTK). The terms on the right side of Eq. (11) represent the horizontal flux divergence (HFD), vertical flux divergence (VFD), horizontal generation (HGE), vertical generation (VGE), total buoyancy production (BUP) and the dissipation (FDI) of kinetic energy, respectively.  $q_r$  is the rain water mixing ratio.

Figure 16 shows the vertical profiles of LTK at earlier times of the rainstorm. The growth of kinetic energy appears to have been initiated in the lower troposphere below 5 km, and then spread upward to the upper troposphere. The growth of kinetic energy grew fastest at the 3-km level in the lower troposphere and 8-km level in the upper troposphere, respectively.

In order to further understand the details of the formation of the kinetic energy, each term in Eq. (11) were computed every 5 min at times from 2200 UTC 10 September 2010 to 0300 UTC 11 September 2010. FDI was excluded according to calculation results because its magnitude was so small that it could be ignored.

Figure 17a shows that the low-level growth of kinetic energy started from 2325 UTC 10 September 2010, and peaked round 0050 UTC 11 September 2010, corresponding to the 1-hour rainfall maxima. In the whole process, neither HFD nor VFD made any contribution to kinetic energy growth. From 2325 UTC 10 September 2010 to 0000 UTC 11 September 2010, HGE was the major source, although its value was small. Equation (11) shows that HGE is a function of horizontal wind velocity and horizontal gradient of

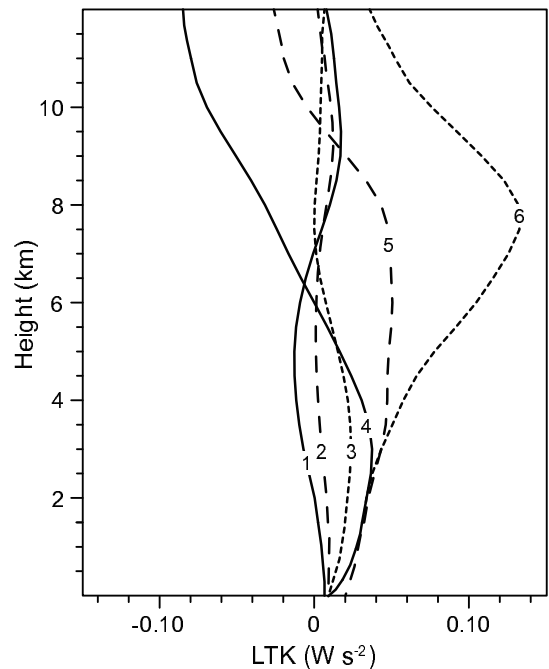


**Fig. 16.** The development of rainstorm-area mean LTK ( $\text{W s}^{-2}$ ). The numbers 1–6 beside the curves represent times at 2315 UTC, 2325 UTC, 2335 UTC, 2340 UTC, 2345 UTC, and 2350 UTC 10 September 2010 respectively.

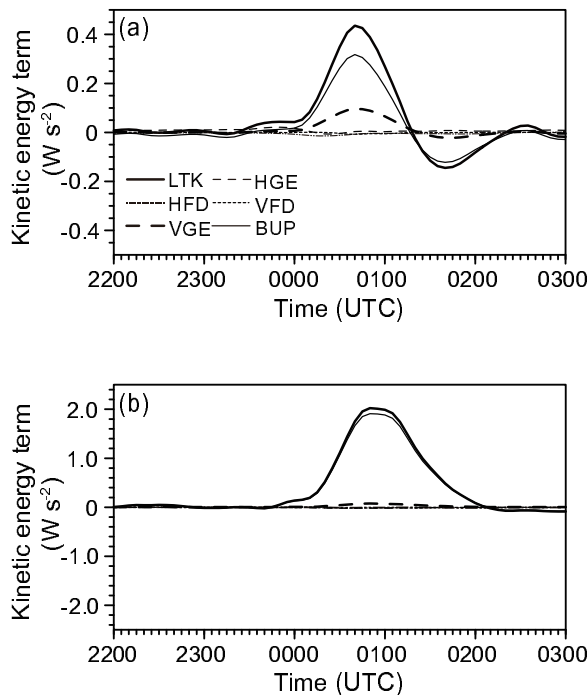


**Fig. 17.** Time variation of each term in the kinetic energy budget in the rainstorm area at the (a) 3-km level and (b) 8-km level. The plots show LTK (heavy solid line), HFD (dot-dashed line), VFD (dotted line), HGE (light short-dashed line), VGE (heavy long-dashed line), BUP (light solid line). FDI of kinetic energy was neglected due to its small magnitude.

pressure perturbation. The pressure perturbation was almost constant at around 400 Pa at 3-km high, so it was impossible for HGE to achieve a large increase. The most positive HGE was brought about by the low-level jet (Fig. 18). The above discussions have mentioned that the jet was the southwesterly jet from the western margin of the Subtropical High. It flew into the remnant clouds under the force of a pressure gradient. After 0000 UTC 11 September 2010, VGE and BUP provided almost all the positive contribution to kinetic energy growth (Fig. 17a). Figure 18 shows that the pressure perturbation gradient was large and negative below 5-km high. The upward movement in the lower levels was forced by the lifting of cold air, such that the vertical velocity at 3-km high was relatively small. Thus, VGE made a moderate contribution to the growth of kinetic energy. BUP is not only affected by vertical velocity but also heat and moisture [Eq. (11)]. The low-level southwesterly jet brought about plenty of moisture and heat from the ocean and created buoyancy, which in turn forced air upward and converted directly to kinetic energy. Therefore, the source of BUP became the biggest source for kinetic

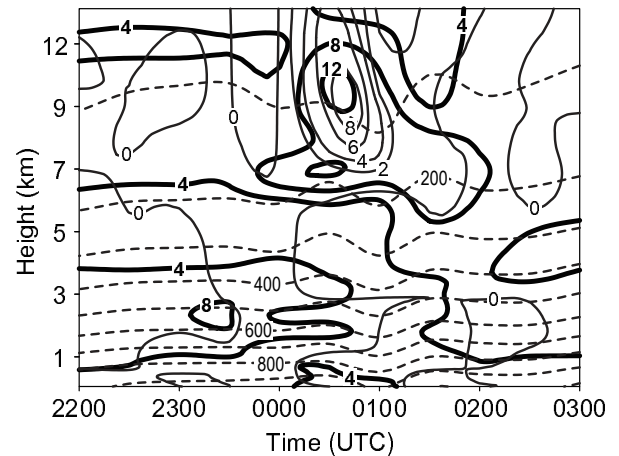


**Fig. 18.** Time variation of rainstorm-area mean horizontal wind velocity (bold solid lines, contour interval of 4 m s<sup>-1</sup>), vertical wind velocity (thin lines, contour interval of 2 cm s<sup>-1</sup>), and pressure perturbation (dashed lines, contour interval of 100 Pa).

energy growth in the lower levels, and was very important for the development of convective storms (Lin et al., 1988). In the upper levels, the composition was simpler: 90% of the kinetic energy growth was provided by BUP, and the remaining 10% came from VGE. Compared with the low-level kinetic energy budget, the value in the upper levels was nearly ten times bigger (Fig. 17b), because vertical velocity was very large at 8-km high. Therefore, the contribution from VGE was negligible.

## 8. Conclusion

The ARW model was used to simulate a sudden extreme rainstorm associated with the remnant clouds of Typhoon Meranti in September 2010. The results showed that:

(1) The heavy rainfall was produced when the remnant clouds redeveloped suddenly, and the redevelopment was caused by rapid growth of MCSs inside the remnant clouds. As cold air from the north intruded into the warm remnant clouds, the atmosphere became convectively unstable and frontogenesis occurred due to strong wind shear between weak northerly flow and strong southerly flow in the lower levels. Under frontogenesis forcing and warm-air advection stimulation in updrafts, vertical convection developed intensely inside the remnant clouds, with MCSs forming and maturing along the front.

(2) The genesis and development of MCSs was due to the great progress vertical vorticity made. When cold air intruded, the moist isentropic surface became

slantwise as atmospheric baroclinity intensified, which reduced the convective instability of the air. At the same time, vertical wind shear increased because the northerly cold air caused the wind direction to turn from south to north with height. According to SVD, vertical vorticity would then have developed vigorously and contributed greatly to MCSs.

(3) Buoyancy, pressure gradient and cold-air lifting were the sources of kinetic energy for rainfall. The growth of kinetic energy first initiated in the lower levels, and then spread to upper levels, sometimes in less than an hour. The low-level southwesterly jet from the western margin of the Western Pacific Subtropical High continued to transport plenty of water and heat to remnant clouds for several hours. Energy bursts and continuous water vapor transportation played a major role in producing intense rainfall that fell in a very short period of time.

**Acknowledgements.** The authors would like to thank HE Bin for the TBB data, and YANG Jun for the Doppler radar data. This work was supported by the General Program of the National Natural Science Foundation of China (Grant No. 40975021), the 2012 General Program of the State Key Laboratory of Disaster Weather, the National Department Public Benefit Research Foundation (Grant No. GYHY201006007), and the Major Science and Technology Project of Zhejiang Province Science and Technology Department (Grant No. 2011C13044).

## REFERENCES

- Betts, A. K., 1986: A new convective adjustment scheme. Part I: Observational and theoretical basis. *Quart. J. Roy. Meteor. Soc.*, **112**, 677–691.
- Betts, A. K., and M. J. Miller, 1986: A new convective adjustment scheme. Part II: Single column tests using GATE wave, BOMEX, and arctic air-mass data sets. *Quart. J. Roy. Meteor. Soc.*, **112**, 693–709.
- Bosart, L. F., and D. B. Dean, 1991: The Agnes rainstorm of June 1972: Surface feature evolution culminating in inland storm redevelopment. *Wea. Forecasting*, **6**, 515–537.
- Chen, L., 2006: Observations and forecasts of rainfall distribution. *Proc. Sixth Int. Workshop on Tropical Cyclones*, San Jose, Costa Rica, WMO, 36–42.
- Chen, L., and Z. Meng, 2001: An overview on tropical cyclone research progress in China during the past ten years. *Chinese J. Atmos. Sci.*, **25**, 420–432. (in Chinese)
- Chen, L., and Z. Luo, 2004: A study of the effect of topography on the merging of vortices. *Adv. Atmos. Sci.*, **21**, 13–22.
- Cheng, Z., L. Chen, Y. Liu, and T. Peng, 2007: The spatial and temporal characteristics of tropical cyclone induced rainfall in China during 1960–2003. *Journal of Applied Meteorological Science*, **18**, 427–434. (in Chinese)
- Dong, M., L. Chen, Y. Li, and C. Lu, 2010: Rainfall reinforcement associated with landing tropical cyclones. *J. Atmos. Sci.*, **67**, 3541–3558.
- Du, H., X. Huang, X. Feng, and D. Teng, 2011: The effect of the interaction between weak cold flow and typhoon depression on a rainstorm. *Meteorological Monthly*, **37**, 847–856. (in Chinese)
- Du, X., Z. Yu, C. Lu, and Y. Wang, 2007: A research on the mechanism for the Shanghai heavy rainfall event on 5–6 August 2001 caused by a tropical depression. *Journal of Nanjing University (Natural Sciences)*, **43**, 621–632. (in Chinese)
- Duan, L., and L. Chen, 2005: Diagnostic analysis and numerical study of torrential rain associated with the tropical storm Fitow (0114). *Chinese J. Atmos. Sci.*, **29**, 343–353. (in Chinese)
- Duan, X., and Y. Li, 2000: Diagnostic analysis of moist potential vorticity for heavy rain in middle Yunnan. *Plateau Meteorology*, **19**, 253–259. (in Chinese)
- Emanuel, K. A., 1983: The Lagrangian parcel dynamics of moist symmetric instability. *J. Atmos. Sci.*, **40**, 2368–2376.
- Emanuel, K. A., 1988: Observational evidence of slantwise convective adjustment. *Mon. Wea. Rev.*, **116**, 1805–1816.
- Gao, S., Z. Meng, F. Zhang, and L. F. Bosart, 2009: Observational analysis of heavy rainfall mechanisms associated with severe Tropical Storm Bilis (2006) after its landfall. *Mon. Wea. Rev.*, **137**, 1881–1897.
- Han, G., X. Tang, and J. Wei, 2007: The extratropical transition analysis on two landfall typhoons. *Scientia Meteorologica Sinica*, **27**, 35–41. (in Chinese)
- Holton, J. R., 2004: An introduction to dynamic meteorology. 4th ed., *Int. Geophys. Ser.*, Vol. 88, Academic Press, USA, 164–168.
- Hong, S. Y., and J. Dudhia, 2003: Testing of a new non-local boundary layer vertical diffusion scheme in numerical weather prediction applications. *20th Conference on weather analysis and forecasting/16th conference on numerical weather prediction*, Seattle, WA., 6.
- Hoskins, B. J., and M. A. Pedder, 1980: The diagnosis of middle latitude synoptic development. *Quart. J. Roy. Meteor. Soc.*, **106**, 707–719.
- Hoskins, B. J., I. Draghici, and H. C. Davies, 1978: A new look at the omega equation. *Quart. J. Roy. Meteor. Soc.*, **104**, 31–38.
- Janjic, Z. I., 1994: The step-mountain eta coordinate model: Further developments of the convection, viscous sublayer, and turbulence closure schemes. *Mon. Wea. Rev.*, **121**, 927–945.
- Kong, K., 2002: Anomalous intensification of the remnants of tropical storm Allison overland. *25th conf. on Hurricane and Tropical Meteorology*, San Diego, AMS, 9–10.
- Li, S., and S. Shou, 1995: Energetic analysis of maintenance and rainfall amplification of landed typhoons.

- Journal of Nanjing Institute of Meteorology*, **18**, 383–388. (in Chinese)
- Li, Y., and S. Shou, 2000: A study on MPV and symmetric instability during a torrential rain process. *Scientia Meteorologica Sinica*, **20**, 172–178. (in Chinese)
- Li, Y., L. Chen, and J. Wang, 2005: Diagnostic study of the sustaining and decaying of tropical cyclones after landfall. *Chinese J. Atmos. Sci.*, **29**, 482–490. (in Chinese)
- Li, Y., L. Chen, and X. Lei, 2008: Frontogenesis in the circulation of typhoon Winnie (1997) during its extratropical transition process. *Chinese J. Atmos. Sci.*, **32**, 629–639. (in Chinese)
- Lin, Y. J., and J. A. Coover, 1988: A kinetic energy analysis of a microburst-producing thunderstorm based on JAWS dual-Doppler data. *J. Atmos. Sci.*, **45**, 2764–2771.
- Lin, Y. L., R. D. Farley, and H. D. Orville, 1983: Bulk parameterization of the snow field in a cloud model. *J. Appl. Meteor. Climatol.*, **22**, 1065–1092.
- Lin, Y. J., R. G. Hughes, and R. W. Pasken, 1988: Subcloud-layer kinematic and dynamic structures of a microburst-producing thunderstorm in Colorado determined from JAWS dual-doppler measurements. *Bound.-Layer Meteor.*, **39**, 67–86.
- Palmen, E., 1958: Vertical circulation and release of kinetic energy during the development of hurricane hazel into an extratropical storm. *Tellus*, **10**, 1–23.
- Qi, L., and S. Zhao, 2004: An analysis of mesoscale features of heavy rainfall in Shanghai on 5–6 August 2001. *Chinese J. Atmos. Sci.*, **28**, 254–268. (in Chinese)
- Rutledge, S. A., and P. V. Hobbs, 1984: The mesoscale and microscale structure and organization of clouds and precipitation in midlatitude cyclones. XII: A diagnostic modeling study of precipitation development in narrow cold-frontal rainbands. *Atmos. Sci.*, **20**, 2949–2972.
- Sanders, F., and L. F. Bosart, 1985: Mesoscale structure in the megalopolitan snowstorm of 11–12 February 1983. Part I: Frontogenetical forcing and symmetric instability. *J. Atmos. Sci.*, **42**, 1050–1061.
- Shou, S., Y. Li, and K. Fan, 2001: Isentropic potential vorticity analysis of the mesoscale cyclone development in a heavy rain process. *Acta Meteorologica Sinica*, **59**, 560–568. (in Chinese)
- Tao, W. K., 1989: An ice-water saturation adjustment. *Mon. Wea. Rev.*, **117**, 231–235.
- Wu, G., Y. Cai, and X. Tang, 1995: Moist potential vorticity and slantwise vorticity development. *Acta Meteorologica Sinica*, **53**, 387–405. (in Chinese)
- Xu, X., L. Gao, and F. Jin, 2009: The wave capture mechanism of the genesis and development of the mesoscale convective systems in the Meiyu moist front. *Progress in Natural Science*, **19**, 1203–1208. (in Chinese)
- Yan, J., J. Xu, W. Ding, Z. Chen, and Y. Liao, 2005: A modeling study of the impact of terrain on the intensity of landfalling tropical cyclone Vongfong (0214). *Chinese J. Atmos. Sci.*, **29**, 205–212. (in Chinese)
- Yang, Y., Y. Zheng, and Z. Tao, 2003: Analysis of tropical depression rainstorm in Shanghai. *Journal of Tropical Meteorology*, **19**, 413–421. (in Chinese)
- Yang, Y., X. Zhu, and Z. Tao, 2011: Numerical simulation of tropical depression structure in Shanghai torrential and its intensifying analysis. *Plateau Meteorology*, **30**, 416–427. (in Chinese)
- Zhang, X., A. Xu, and X. Liu, 2009: A diagnostic case study on the interaction between mid-latitude trough and tropical depression “Neoguri”. *Journal of Tropical Meteorology*, **25**(Suppl.), 29–38. (in Chinese)